Compressive Sensing Techniques for the Detection of Surface Waves

Koen Blaauw
Department of Electromagnetics,
Energy Management & Qualification
Royal Netherlands Aerospace Center
Marknesse, The Netherlands
koen.blaauw@nlr.nl

Harmen van der Ven
Department of Flight
Physics & Loads
Royal Netherlands Aerospace Center
Amsterdam, The Netherlands
harmen.van.der.ven@nlr.nl

***Abstract*— Understanding the scattering physics of specific objects is important for their design and use. Imaging techniques may give this insight, provided that they can distinguish different scattering mechanisms. The use of compressive sensing (CS) in imaging allows to use different scattering models. In this paper, two models for surface wave (SW) scattering are described and applied to a canonical test case. We find that CS is effective in extracting the reflection of surface waves from the total radar echo. However, the standard ℓ_1-regularization of the CS optimization problem requires careful balancing of the different scattering models. It is shown that the Bayesian approach to solve the CS optimization problem does not suffer from this problem.**

Keywords*— *surface waves, imaging techniques, scattering, compressive sensing.

I. INTRODUCTION

The radar signature of a platform is determined by a variety of scattering mechanisms, including specular reflection, edge diffraction, and reflections from surface and creeping waves. Since different mechanism might require a unique method of mitigation [1], the ability to extract, quantify and locate the reflection of individual scattering mechanisms from the total radar echo, serves great purpose for the design and use of low-observable platforms.

While radar imaging is commonly used to assess the reflection properties of a target, conventional inverse synthetic aperture radar (ISAR) cannot differentiate between different scattering mechanisms. In contrast, the use of compressive sensing (CS) in imaging, allows for the parallel use of different scattering models. This idea was first proposed by LaHaie and his co-workers [2], who used different models for clutter and target support to extract a clean radar image from measurements. In a later paper [3], they developed a model (which they call basis) for the scattering return of inlets, to distinguish the inlet scattering from specular scattering; a finite number of point scatterers in the 'wake' of the inlet are added which only radiate towards the inlet. Additionally, Lee [4] introduced a model for diffraction scattering to improve the performance of imaging techniques (in terms of the sparsity of the image). The diffraction scatterers are no longer isotropic: their amplitude depends on frequency and aspect.

The purpose of the current paper is to develop an imaging technique to distinguish surface wave scattering from other scattering mechanisms. As surface waves may already occur on finite wires, an obvious approach is to add a model in which point scatterers are replaced with line scatter centers (SCs) of which the amplitude depend on frequency and aspect. Two such models will be considered. One of the models is based on the same principles as the traveling wave scatter centers model of Zhao [5].

Compressive sensing is an effective technique to generate sparse solutions to inverse problems (see [6] for a general introduction and [7] for a review of its application to electromagnetics). The standard approach to solve the CS optimization problem is to relax the sparsity driven ℓ_0-norm to the ℓ_1-norm. In this paper this is called the deterministic approach.

In case deterministic CS is used with multiple models, then ℓ_1-regularization requires some balancing of the models. In its attempt to minimize the ℓ_1-norm, the CS algorithm will favor the 'heavier' models, that require smaller amplitudes. Consequently, an optimal sparse solution will not be obtained. To the authors' knowledge, there does not exist a metric to determine the weights of the different models.

The issue of balancing models is not mentioned in literature. The models of LaHaie et al. are in essence point scattering models and may be naturally balanced. The diffraction model of Lee is not a point scattering model. Interestingly, Lee applies CS to the isotropic point scattering model only and uses prior knowledge to define location and strength of the diffraction scatterers.

The novelty in the present paper is twofold. First, a new imaging technique is presented that uses both a point scatterer model and a surface wave model with the aim to extract the contribution of surface waves from the total radar echo. Second, it is demonstrated that the so-called Bayesian approach [8] to solve the CS optimization problem is superior to the deterministic approach which relies on ℓ_1-regularization.

The paper is organized as follows. Section II serves as a short introduction on the use of compressive sensing for imaging. In Section III the physics of surface waves is briefly discussed and two surface wave models are presented. In Section IV deterministic and Bayesian CS are used to extract the surface waves for the canonical test case of a metal plate. Finally, in Section V some conclusions are drawn.

II. COMPRESSED SENSING RADAR IMAGING

Usually, a radar image is reconstructed from radar cross section (RCS) measurements by approximating the scene by a finite number of isotropic point scatterers. The goal is to assign a complex amplitude to each scatterer such that the collective return approaches the measured field. Mathematically, let N point scatterers at locations $\boldsymbol{r}_j$ have an amplitude $z_j \in \mathbb{C}$, then the scattered farfield E_s is given by

$$E_s(k,\hat{\mathbf{r}}) = \sum_{j=1}^{N} z_j e^{-2ik\mathbf{r}_j\cdot\hat{\mathbf{r}}}\ , \tag{1}$$

for the wave number k and direction $\hat{\boldsymbol{r}}$**.** A classical ISAR image is obtained by inverting (1) with Fourier transforms, where it is assumed that the left hand side of (1) is available as a measured or calculated field.

Alternatively, the amplitudes, z_j, in (1) can be solved by means of compressive sensing (CS), which is a relatively new methodology in the field of imaging. CS relies on the assumption that many physical phenomena are in essence sparse; so that they can be represented by a few nonzero expansion coefficients with respect to a suitable expansion basis [6]. In mathematical terms, CS tries to solve the following problem:

$$\mathbf{Az} = \mathbf{b}\ , \tag{2}$$

where $\mathbf{A}$ is the forward operator (that is, the exponential term in equation (1)), $\mathbf{z} = \mathbf{z}(x,y)$ contains the scatterer amplitudes to be recovered and $\mathbf{b} = \mathbf{b}(k,\hat{\boldsymbol{r}})$ is the measured field. In most practical cases (2) is underdetermined and therefore ill-posed; the number of unknown coefficients in $\boldsymbol{z}$ exceeds the number of measurements in $\mathbf{b}$. Assuming sparsity in $\boldsymbol{z}$, the problem is regularized by reformulating it as

$$\text{minimize } \|\mathbf{z}\|_0 \text{ subject to } \|\mathbf{Az}-\mathbf{b}\|_2 < \sigma\ , \tag{3}$$

where $\|\boldsymbol{x}\|_0$ is the ℓ_0-norm, counting the non-zeroes in $\boldsymbol{x}$, and $\|\boldsymbol{x}\|_2$ is the ℓ_2-norm or root-mean-square norm and σ is an estimate of the noise level. By promoting sparsity, CS images are reported to provide superior resolution, and suppress noise compared to conventional radar images [7].

Another benefit of reformulating radar imaging as a linear optimization problem is the flexibility in choosing the forward operator. As first proposed by LaHaie [3], multiple forward operators $\mathbf{A}_i$ can be combined into an operator dictionary as

$$\begin{bmatrix}\mathbf{A}_1 & \mathbf{A}_2 & \cdots & \mathbf{A}_N\end{bmatrix}\begin{bmatrix}\mathbf{z}_1\\ \mathbf{z}_2\\ \vdots\\ \mathbf{z}_N\end{bmatrix} = \mathbf{b}. \tag{4}$$

As sparsity is promoted, the CS algorithm populates those sub-vectors $\mathbf{z}_i$ whose corresponding forward operators $\mathbf{A}_i$ describe the measurement data most efficiently. Provided that correct and efficient physical models can be defined for each, this method enables differentiation between various scattering mechanisms,

The major mathematical complication of the CS formulation in (3) is the ℓ_0-norm: the optimization problem is non-convex, and in general the solution can only be found by brute force. There are two approaches to resolve this: the deterministic and the Bayesian approach.

A. Deterministic approach

Under a certain condition on the matrix $\mathbf{A}$, the ℓ_0-norm can be 'relaxed' the to the ℓ_1-norm, $\|\mathbf{x}\|_1 = \sum|\mathrm{x}_i|$, which makes the optimization problem tractable, and still produces a correct and sparse solution for the original problem. The condition is that $\mathbf{A}$ satisfies the restricted isometry property (RIP), which, phrased loosely, is that the matrix (almost) preserves lengths hoi for sparse vectors. Mathematically, there is a constant δ $(0 < \delta < 1)$ such that

$$1-\delta \le \frac{\|\mathbf{Az}\|_2}{\|\mathbf{z}\|_2} \le 1+\delta\ , \tag{5}$$

for all sparse $\boldsymbol{z}$. The constant measures the deviation from isometry: if it is zero, the matrix preserves length. Theory states that the larger δ, the more measurements are needed to reconstruct the solution.

The isometry condition can be explained as follows. Split the matrix into two arbitrary column blocks: $\mathbf{A} = (\mathbf{A}_1\ \mathbf{A}_2)$, and the solution vector likewise: $\mathbf{z} = (\mathbf{z}_1, \mathbf{z}_2)$. If we replace the matrix $\mathbf{A}$ with a partially scaled matrix $\mathbf{A}' = (\mathbf{A}_1\ c\mathbf{A}_2)$, for a constant c, the solution will scale likewise. If $\mathbf{z} = (\mathbf{z}_1, \mathbf{z}_2)$ is the solution for $\mathbf{A}$, then $\mathbf{z}' = (\mathbf{z}_1, \mathbf{z}_2/c)$ will be the solution for $\mathbf{A}'$. Now, both solutions have the same ℓ_0-norm, but their ℓ_1-norms are different. When optimization for the matrix $\mathbf{A}'$ is performed in the ℓ_1-norm, and $c > 1$, the algorithm will put more weight on the second part of the solution vector since that part contributes less to the ℓ_1-norm. So the algorithm may find a different solution for $\mathbf{A}'$ than for $\mathbf{A}$ which shows that the balance between the columns has effect on the solution. Control of the balance is taken care of by the isometry condition. Unfortunately, it is rather difficult to ascertain if a matrix satisfies the isometry condition.

B. Bayesian approach

It is an assumption that the solution is sparse. An assumption is called a prior in Bayesian probability theory and the concept of prior is central to this theory. Therefore, it is no surprise that the CS problem can also be solved with Bayesian techniques. The Bayesian approach is equivalent to minimize $\|\mathbf{Az}-\mathbf{b}\|_2 + \gamma\|\mathbf{z}\|_p^p$ for $0 < p < 1$ (Yang et al. [8]). By choosing a small value of p the solution is forced to be sparse. Since in this approach the ℓ_0-norm is relaxed to an ℓ_p-norm rather than the ℓ_1-norm, it is expected that the Bayesian approach is less susceptible to the balancing of the columns in the matrix $\mathbf{A}$.

III. SURFACE WAVES

Incident radar waves can excite traveling current waves that propagate along the surface of an object. Each wave follows the surface until it reaches a discontinuity, such as an edge or vertex, at which the wave is diffracted. Part of the energy is reflected, giving rise to a backward traveling wave, and part of the energy is radiated in other directions, partially propagating back towards the radar. Although the energy is radiated into multiple directions, the intensity of the radiation towards the radar can be significant, especially once specular reflections have been minimized by shaping or by applying radar absorbing materials.

The effect of surfaces waves on the radar echo is demonstrated by considering a canonical test case; the monostatic reflection from a conducting flat metal plate of length L = 288 mm, lying in the xy-plane as shown in Fig 1. The scattered field was simulated as a function of aspect θ (varied between -10° and 80° with a step size of 0.75°) and frequency (varied between 3 and 17 GHz with a step size of 140 MHz) for both TM_z and TE_z polarization.

The simulated RCS patterns are shown in Fig. 2. The specular return at normal incidence as well as the sinc pattern, characteristic for a uniformly illuminated aperture as described by physical optics (PO), are clearly observed for both polarizations. The difference between both images are

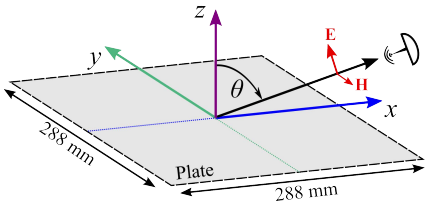

Fig. 1 Schematic of the simulation setup. Field here shown with TM_z polarization.

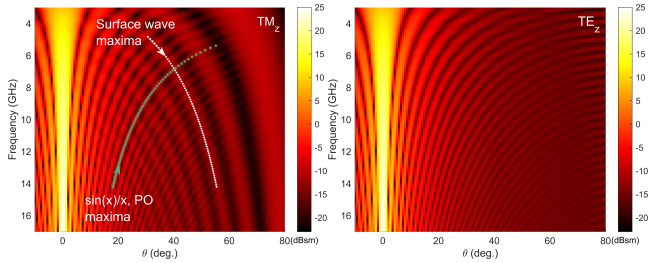

(a) (b)

Fig. 2 Comparison of the simulated RCS of a flat conducting plate for (a) TM_z and (b) TE_z polarization.

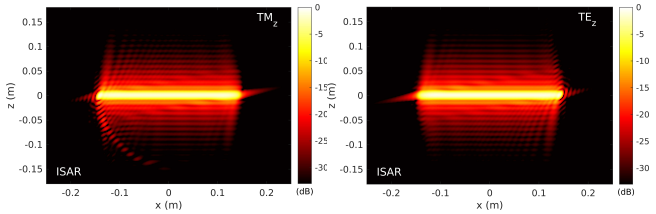

(a) (b)

Fig. 3 Comparison between ISAR images of a flat, conducting plate for (a) TM_z and (b) TE_z polarization.

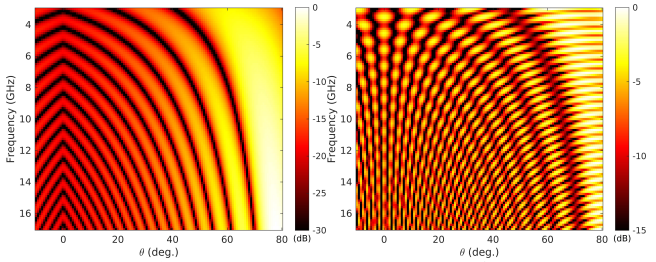

(a) (b)

Fig. 4 The scattered field of a single Stoyanov SC (left) and a single Ross SC (right).

the additional maxima observed in Fig. 2(a) and highlighted by the white line. These maxima are attributed to surface waves which, as pointed out by Knott [1], are only excited when the incident field has a component in the plane of incidence (spanned by the surface normal and the wave propagation vector). For the current setup, the latter is true for TM_z polarization. Note that near grazing incidence, surface waves dominate the target RCS.

The scattered fields from Fig. 2 were used to create the ISAR images shown in Fig. 3. Since frequency and θ were varied, the ISAR image shows a projection of the plate in the xz-plane. Although in both Fig. 3(a) and (b) the plate is clearly visible, an additional arc of scatterers is observed in the image for TM_z polarization. This arc is an artifact attributed to surface waves which obtained a phase delay while flowing on the surface, before scattering back towards the radar. As ISAR imaging is based on a single-bounce assumption of the scattered wave, delayed signals are incorrectly mapped in the image. Based on simple geometry and assuming that the surface wave velocity is equal to the speed of light, first-order surface waves (i.e. waves that propagated along the full length of the plate once) shall appear as an arc, tracing a circular path of radius $L/2$ centered at the center of the plate [5].

In this work, we propose to extract the surface wave contribution from the total radar echo by adding a surface wave model to operator dictionary defined in (4). The surface wave model is supplement to the standard point scatter model. The hypothesis is that while point scatterers are most efficient in reconstructing '*direct'*, PO-like reflection, surface wave models are better suited for reconstructing '*delayed*' reflection from diffracted or reflected surface waves. To identify the most accurate and most efficient surface wave description, two different surface wave models are considered.

A. Stoyanov model

The Stoyanov surface wave model is based on the analogy between the non-specular reflection from a long thin rod and the emitted field of traveling wave antenna [9]. As both phenomena stem from a traveling current wave, the resulting fields are found to be remarkably similar. Therefore, Stoyanov proposes a surface wave description based on the theory of a traveling wave antenna.

In this framework, consider a traveling wave antenna of length L, oriented along the x-axis and centered at the origin. At $x = -L/2$, the antenna is fed by an alternating current

$$I(x) = I_0 e^{ik\left(x+\frac{L}{2}\right)}, \tag{6}$$

running in the +x direction. In the xz-plane, the only non-zero component of the field is the polar component which can be calculated to be proportional to

$$F^S(k,\theta,L) = e^{ik\frac{L}{2}(1+|\sin\theta|)}\frac{\cos\theta}{(1+|\sin\theta|)}2\sin(\alpha), \tag{7}$$

where $\alpha = kL/2\,(1-|\sin\theta|)$. This model is applied in a linear operator describing a grid of N Stoyanov SCs as

$$E_s^S(k,\hat{\mathbf{r}}) = \sum_{j=1}^{N} z_j F^S e^{-2ik\mathbf{r}_j\cdot\hat{\mathbf{r}}}. \tag{8}$$

B. Ross model

Based on the geometrical theory of diffraction (GTD), Ross [10] developed a series expansion in diffraction terms for the radar signature of a flat plate. Consider a flat plate of length L, oriented as shown in Fig. 1. Ignoring the physical optics term, the first three orders of diffraction terms are given as:

$$F^R(k,\theta,L) = \cos\alpha - \frac{4\beta}{\cos\theta} - 2\beta^2\left(\frac{e^{-i\alpha}}{1-\sin\theta}+\frac{e^{+i\alpha}}{1+\sin\theta}\right), \tag{9}$$

where $\alpha = kL\sin\theta$ and $\beta = \exp(ikL+\pi i/4)/\sqrt{2\pi kL}$. This model is applied in a linear operator describing a grid of N Ross SCs as

$$E_s^R(k,\hat{\mathbf{r}}) = \sum_{j=1}^{N} z_j F^R e^{-2ik\mathbf{r}_j\cdot\hat{\mathbf{r}}}. \tag{10}$$

The normalized fields of a single Stoyanov SC and a single Ross SC are shown in Fig. 4(a) and (b) respectively. In both images, the surface wave resonances are clearly visible. Since the Ross scatterer describes multiple orders of diffraction, the scattered field is more involved.

IV. RESULTS

The surface wave extraction method is validated against the simulated scattered field from the square conducting metal plate, shown in Fig. 1, for TM_z polarization.

A. Deterministic CS

This section discusses results obtained using the deterministic approach, employing the compressive sensing method Basis Pursuit Denoise (BPDN) implemented in SPGL1 [11].

As a reference, Fig. 5(a) presents the image obtained using only point scatterers. The result is similar to Fig. 3(a), but due to the sparse nature of CS images, sidelobes are highly oppressed which enhances the visibility of the SW arc. Fig 5(b) shows the simulated RCS pattern versus θ, along with the CS reconstruction at 8 GHz. Note that despite lacking a SW model, the CS algorithm reconstructs the SW lobes, apparent beyond θ =40°, well. The result highlights that the point scatterer model is not able to differentiate between scattering mechanisms, resulting in artefacts such as the SW arc in radar images.

Next, the CS problem was solved using an operator dictionary containing both point scatterers and surface wave scatter centers (SWSCs). The Ross and Stoyanov model were tested sequentially. To reduce the problem size, the SWSCs were restricted to be oriented parallel to, and match the length of the plate such that the algorithm only determines the presence and the location of a SWSC. Be aware that, despite the fact that SWSCs describe the reflection of an object with length, radar images only show activated centers such that also SWSCs are visible as dots.

Fig. 6 shows results obtained using a dictionary including the Ross (left), and the Stoyanov (right) model. The results in both columns show that the SW arc has disappeared in the point scatterer images (Fig. 6(a)) while a bright dot has appeared in the SW images (Fig. 6(b)). This observation demonstrates that different scattering mechanisms are successfully assigned to the appropriate model; Direct reflection is reconstructed using point scatterers, while SW reflection is captured by a SWSC at the origin, overlapping with the plate.

The contribution of each scattering mechanism to the total radar echo is obtained by multiplying each image with its corresponding operator. The results are shown in Fig. 6(c). In both cases, the point model curve exhibits sinc-like behavior, extending up to larger angles θ compared to Fig. 5(b). Towards grazing incidence, the SW curves gradually start dominating the reconstruction of the scattered field. As the Ross model describes up to three orders of diffraction, its corresponding curve is more involved than the Stoyanov curve. The higher number of diffraction orders described by Ross could also account for the fact that larger fraction of the total field is reconstructed by the Ross model in comparison to the Stoyanov model (0.57% and 0.30% respectively).

The distinction of surface wave scatterers from point scatterers is one of the major results of this paper. However, the results with deterministic CS are obtained by a subjective and lengthy process. A user-defined scaling factor, applied to the surface wave model, is iteratively adjusted to obtain the best visual result. As outlined in section II.A., the need to balance operators is inherent to the deterministic approach. This is not robust and for real-life problems it is not known a priori what the best result is.

B. Balancing of operators

In this section, we demonstrate the balancing issue on a simple set of point scatterers (in the shape shown in Fig. 7(a)). In line with the though experiment described in Section II.A., the forward operator is split into two parts, one for the left part of the image and one for the right part of the image. Subsequently, the operator for the right part of the picture is scaled with a factor *c*.

The results obtained using deterministic CS are shown in Fig. 7. For *c=1.5*, the image still reproduces the point scatterers, but for *c=5* the right part of the image gets blurred, as the algorithm tries to locate more scatterers in this part of the image. For *c=100* (not shown here), the algorithm no longer converges.

The results obtained using Bayesian CS are shown in Fig. 8. Clearly, Bayesian CS does not suffer from the balancing problem: for both scaling factors, the images show a distinct set of point scatterers. Even for *c=100*, the algorithm still converges to the correct sparse solution. These experiments demonstrate that Bayesian CS is insensitive to the weights of different operators, and, as such, ideally suited for imaging using a dictionary of multiple scattering models.

C. Bayesian CS

The results discussed in this section were obtained using the Bayesian compressive sensing algorithm provided by Ji et al [12]. Fig. 9(a) presents the image obtained using only point scatterers. Again, the plate and the SW arc are clearly shown, but Bayesian CS is observed to produce more '*spotty'* images. The image can be improved by computing a classical ISAR image from the radiated field of the point scatterers [13].

Results obtained when including the Ross and Stoyanov model sequentially, are shown in Fig. 10. In line with the deterministic results, the surface wave arc disappears in the point SC image while a number of SWSCs centered around the origin become evident in the surface wave images. The most notable difference between the deterministic and the Bayesian images is that a larger fraction of the radar echo is reconstructed by a surface wave model when using the Bayesian approach (0.73% and 0.38% for Ross and Stoyanov resp.). The difference could indicate that the models were not optimally balanced while using deterministic approach and thereby highlights the advantage of the Bayesian approach.

Finally, the scattered field is reconstructed using an operator dictionary including the point model, as well as both the Ross and the Stoyanov SW models. The results in Fig. 11 are consistent with previous results in the sense that the SW arc is absent in the point scatterer image. Additionally, active SWSCs are evident in both SW images, indicating that the algorithm uses both models to reconstruct the field. Moreover, we observe that the Stoyanov model contributes 0.30% to the total field while the Ross model only contributes 0.09%.

This suggests that the algorithm may favor the Stoyanov model for a particular order of diffraction and utilizes the Ross model to account for the remaining, higher-order reflections. In conclusion, these findings do not indicate a clear preference for one of the two surface wave models which emphasizes the need for experiments on other canonical test cases to identify the superior model.

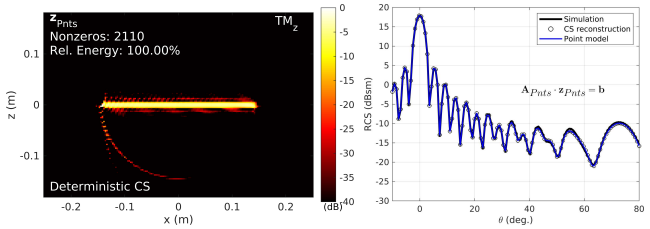

(a) (b)

Fig. 5 (a) Image of the plate using deterministic CS on a dictionary with only point SCs. (b) RCS patterns at 8 GHz.

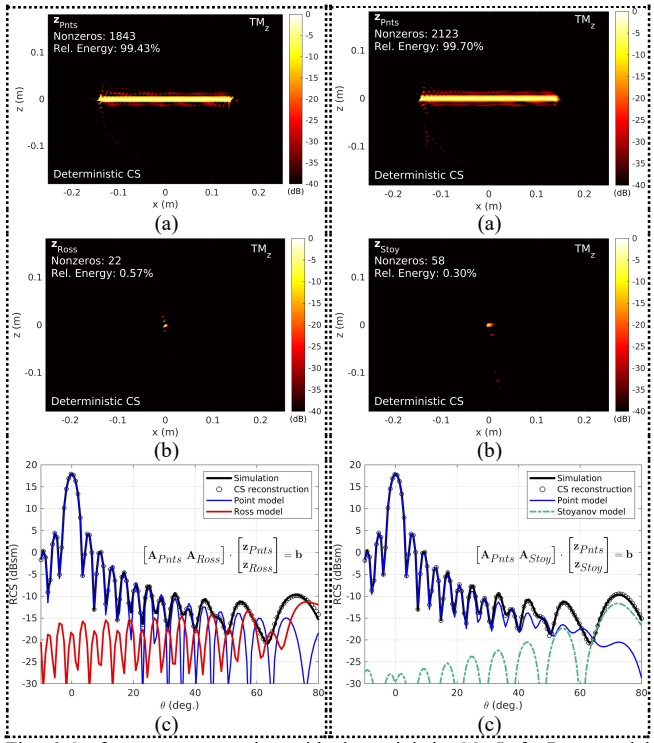

(a) (b) (c)

Fig. 6 Surface wave extraction with deterministic CS. Left: Ross model, Right: Stoyanov model. (a) Point SCs (b) Surface wave SCs (c) RCS patterns at 8 GHz.

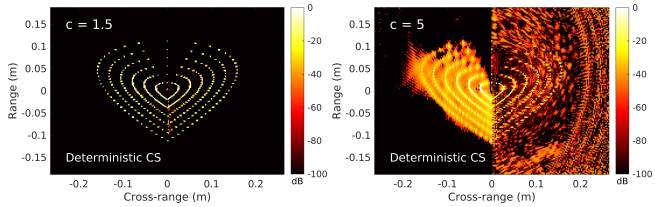

(a) (b)

Fig. 7 Deterministic CS images with scaling factor c applied to the right half of the operator.

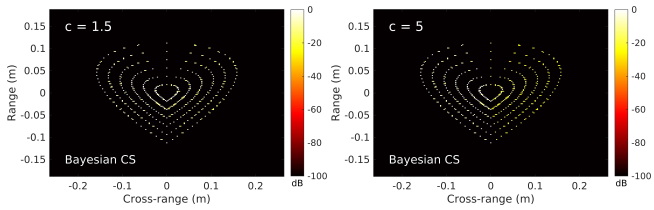

(a) (b)

Fig. 8 Bayesian CS images with scaling factor c applied to the right half of the forward operator **A**.

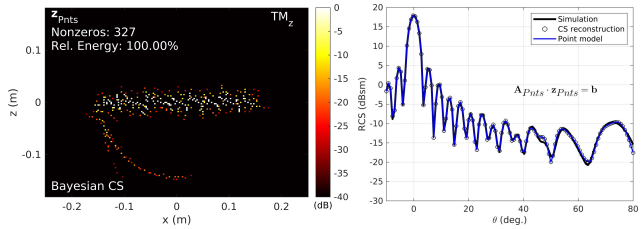

(a) (b)

Fig. 9 (a) Image of the plate using Bayesian CS on a dictionary with only point SCs. (b) RCS pattern at 8 GHz.

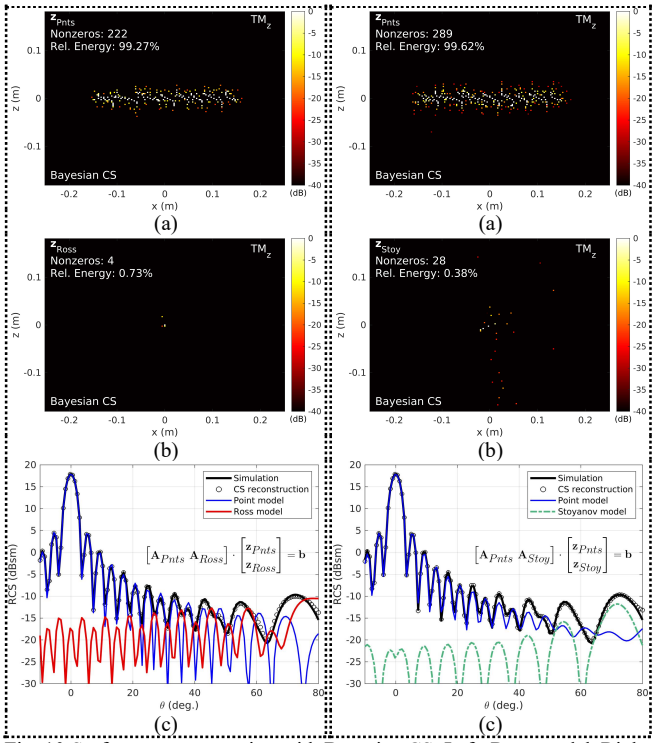

(a) (b) (c)

Fig. 10 Surface wave extraction with Bayesian CS. Left: Ross model, Right: Stoyanov model. (a) Point SCs (b) Surface wave SCs (c) RCS patterns at 8 GHz.

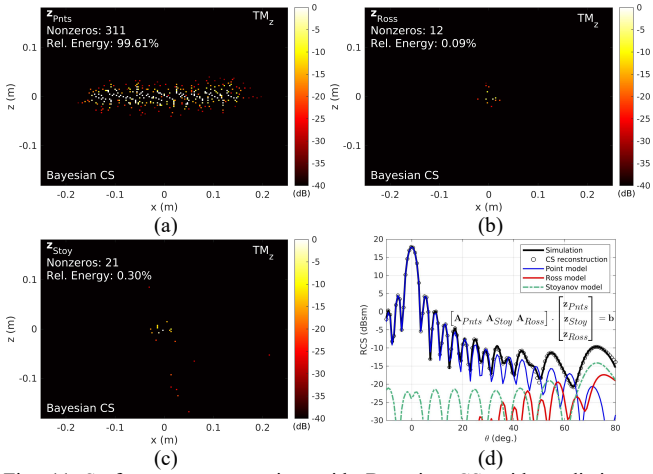

(a) (b) (c) (d)

Fig. 11 Surface wave extraction with Bayesian CS with a dictionary containing both the Ross and the Stoyanov model (a) Point SCs (b) Ross SCs (c) Stoyanov SCs (d) RCS patterns at 8 GHz.

V. Conclusions

The results as presented in the previous section have shown that surface waves can be detected from scatter data. It is obvious that CS is a powerful technique to differentiate between different scattering mechanisms. The approach requires a dictionary of models correctly and efficiently describing different scattering mechanisms. In this research, the point scatterer model is combined with two surface wave models.

Two CS solution techniques have been investigated: the deterministic approach and the Bayesian approach. The standard ℓ_1-regularization of the CS optimization problem requires careful balancing of the different scattering models. If the balancing is incorrect, the deterministic approach will favor one model over the other, resulting in inaccurate, or even corrupt, images. How to balance different models is an open problem. The Bayesian approach does not suffer from this balancing issue and therefore gives accurate images of the contributions of the different models to the scattering of the target.

The developed methods and models have been applied to a canonical test case; a flat plate. The results show that provided a correct SW model, CS is effective in extracting the contribution of surface waves from the total radar echo. To determine the superior surface wave model among the Ross and Stoyanov models considered here, and to determine the applicability of the method on more complex targets, further analysis on additional test cases is required.

Acknowledgment

The research described in this paper has been executed in the EDA project ALOCAS, supported by the Dutch Ministry of Defence under contract EDA B.PRJ.RT.796.

References

[1] E. F. Knott, *Radar Cross Section*, 2nd ed. Raleigh: SciTech Pub, 2004.

[2] B. Fischer, I. LaHaie, M. Hawks, and T. Conn, “On the use of basis pursuit and a forward operator dictionary to separate specific background types from target RCS data, ”*AMTA 36th Annual Meeting and Symposium*,” Tucson, Arizona, 2014, pp. 85-90.

[3] I.J. LaHaie, G. D. Dester and M. H. Hawks, "An Efficient Basis for Decomposition of Cavity Returns in Inverse Synthetic Aperture Radar (ISAR) Measurements Using Basis Pursuit, ”*2019 International Conference on Electromagnetics in Advanced Applications (ICEAA)*,” Granada, Spain, 2019, pp. 0563-0568.

[4] J. Lee, P. J. Collins, and J. A. Jackson, “Sparse Representation of Targets with Mixed Scattering Primitives,” *ACES J.,* Vol. 35, No. 6, June 2020.

[5] X. T. Zhao, K. Y. Guo, Y. X. Chen and X. Q. Sheng, “Traveling Wave Scattering Model and Its Applications to ISAR imaging,” *IEEE. Communications*, vol. 69(4), 2021.

[6] S. L. Brunton and J. N. Kutz, *Data-driven Science And Engineering, Machine Learning, Dynamical Systems And Control*, Cambridge: Cambridge University Press, 2019

[7] A. Massa, P. Rocca, and G. Oliveri, “Compressive Sensing in Electromagnetics – A Review,” *IEEE, Ant. Prop. Mag*., Vol 57 (1), 2015.

[8] J. Yang, T. Jin, C Xiao and X. Huang, “Compressed Sensing Radar Imaging: Fundamentals, Challenges, and Advances,” *Sensors*, **19**, 3100, 2019.

[9] Y. J. Stoyanov, “Radar cross section calculations of traveling surface waves,” DTRC-90/014, David Taylor Research Center, 1990.

[10] R. A. Ross, “Radar Cross Section of Rectangular Flat Plates as a Function of Aspect Angle,” *IEEE Trans. Ant. Prop*. 14(3), 1966.

[11] E. van den Berg and M. P. Friedlander, “SPGL1: A solver for large-scale sparse reconstruction,” 2007, http://www.cs.ubc.ca/labs/scl/spgl1.

[12] S. Ji, and L. Carin, “Bayesian compressive sensing,” *IEEE Transactions on Signal Processing*, vol. 56(6) 2008, https://github.com/shihaoji/bcs.

[13] C. Larsson, “Near to far field transformation of RCS using a compressive sensing method,” *AMTA 2016 Proceedings*, Austin, TX, USA, 2016.